Icarus **144**, 313–328 (2000)
doi:10.1006/icar.1999.6310, available online at http://www.idealibrary.com on IDEAL®

# Lithospheric Loading by the Northern Polar Cap on Mars

Catherine L. Johnson and Sean C. Solomon

*Department of Terrestrial Magnetism, Carnegie Institution of Washington, 5241 Broad Branch Road, N.W., Washington, DC 20015*
E-mail: cjohnson@dtm.ciw.edu

James W. Head III

*Department of Geological Sciences, Brown University, Providence, Rhode Island 02912*

Roger J. Phillips

*Department of Earth and Planetary Sciences, Washington University, St. Louis, Missouri 63130*

David E. Smith

*Geodynamics Branch, NASA Goddard Space Flight Center, Greenbelt, Maryland 20771*

and

Maria T. Zuber

*Department of Earth, Atmospheric, and Planetary Sciences, Massachusetts Institute of Technology, Cambridge, Massachusetts 02139*

Received March 24, 1999; revised December 9, 1999

**New topography data for the northern polar region on Mars, returned by the the Mars Orbiter Laser Altimeter (MOLA) during the aerobraking hiatus and science phasing orbits, allow characterization of the topography of the present northern polar cap and its environs. Models for loading of an elastic shell by an axisymmetric load approximating the present polar cap geometry indicate that the maximum deflection of the subice basement is in the range 1200 to 400 m for an elastic lithosphere of thickness 40 to 200 km overlain by a cap of pure $H_2O$ ice. Corresponding model cap volumes increase from 1.5 to 1.8 $\times$ $10^6$ $km^3$, as elastic lithosphere thickness decreases from 200 to 40 km. The presence of sediments in the polar cap increases the depth to basement and resulting cap volume for a given value of elastic lithosphere thickness. One-dimensional heat flow calculations indicate that the temperature at the base of the cap may approach the melting point of cap material if the lithosphere underlying the cap is thin. The basal temperature is 170 K for a 200-km-thick lithosphere overlain by pure ice but is as great as 234 K for a 40-km-thick lithosphere overlain by a cap with a high sediment/ice ratio. Constraints on elastic lithosphere thickness are weak, but geologic mapping and MOLA data suggest that a flexurally derived circumpolar depression filled with sediments is consistent with elastic lithosphere thickness values in the range 60–120 km. Gravity and topography over the whole cap are poorly correlated, possibly due to viscous relaxation of long-wavelength topography, but gravity and topography over the western portion of the main cap are consistent with an elastic lithosphere thickness of 120 km, for a crustal thickness of 50 km. Both MOLA data and geological information suggest a formerly larger northern polar cap. The relationship of time scales for changes in the polar cap volume and extent to time scales for viscous relaxation of topography has important implications for investigations of even present polar cap topography. Viscoelastic calculations show that the Maxwell time for an Earth-like mantle viscosity for Mars ($10^{21}$ Pa-s) is $10^5$ yr. The Maxwell time scales directly with the martian mantle viscosity so that values as high as $10^7$ yr are possible. Time scales for changes in polar cap volume are poorly constrained, but major changes in cap volume over periods of $10^6$–$10^8$ yr are consistent with current understanding of polar cap processes.** 

*Key Words:* **Mars; ices; geophysics; Mars, climate; Mars, interior.**

## 1. INTRODUCTION

The northern polar cap of Mars is an important volatile reservoir for that planet. The partitioning of volatiles among the polar caps, the atmosphere, and the regolith has changed through time, a consequence of climate changes driven by variations in planetary obliquity (Kieffer and Zent 1992). In particular, the polar caps have likely undergone episodic changes in mass and spatial extent, producing a temporally varying load on the underlying lithosphere. It is difficult to determine the detailed time evolution of the polar caps because of complex feedbacks among climate variations, resulting changes in polar cap volumes, and the influence of the polar caps on planetary dynamics (Rubincam



0019-1035/00 $35.00

1990, 1993; Spada and Alfonsi 1998; Bills 1999). However, new topography and gravity data from the Mars Global Surveyor (MGS) mission (Smith *et al.* 1998; Zuber *et al.* 1998a,b), together with geological information derived from Mariner and Viking images, enable a significant advance in the characterization of the spatial extent, volume, and surface morphology of the present-day northern cap. This information in turn provides constraints for elastic and viscoelastic compensation models for the northern polar cap (this study, Zhong and Zuber 2000), models for the dynamics and recent temporal variations in the cap (Zuber *et al.* 1998a), and investigations of the effect of the current cap on the planet's mass distribution and solid-body dynamics (Zuber and Smith 1999). Further, in combination with climate models (Touma and Wisdom 1993, Bills 1999), the characterization of the present cap and suggestions from topography and image data of a formerly larger cap provide foundations for future studies of the interactions among climate, cap volume, and planetary dynamics over time.

Prior to the MGS mission, knowledge of the topography of the northern polar cap and surrounding regions was derived from regional digital elevation models based on photoclinometry, stereo imaging, and three Mariner 9 occultation measurements (Dzurisin and Blasius 1975, Blasius *et al.* 1982, Esposito *et al.* 1992, Batson and Eliason 1995). These models indicated that the polar deposits are described by a broad topographic high at latitudes northward of 80°N. The thickness of the polar deposits was estimated to average 2 km and to be as great as 5 km (Thomas *et al.* 1992). Wide curvilinear reentrants known as chasmata, some with steep scarps, modify the long-wavelength cap topography. While heights derived from stereo imaging yield high-spatial-resolution information on relative topography within the region defined by the images, long-wavelength topography is not constrained and elevations derived from such information cannot be tied to an absolute global reference frame. Global digital elevation models for Mars (Wu 1989, 1991) also suffer from poor long-wavelength control. Because of the large spatial extent of the cap, long-wavelength information is critical to an accurate estimation of the surface topography of the cap and surrounding regions. Prior to MGS, a degree and order 8 (equivalent to wavelengths of 2700 km and greater) spherical harmonic global topography model derived from radio occultation data and Viking lander sites (Smith and Zuber 1996) provided the best estimate of the long-wavelength shape of Mars.

Polar deposits include the residual or permanent polar cap, seasonal ices, and the polar layered deposits that surround and may underlie the perennial caps. Viking Orbiter Infrared Thermal Mapper data indicate that the composition of the residual northern polar cap is primarily $H_2O$ ice; measurements of the ice albedo suggest that small amounts of dust or sediments are also present (Thomas *et al.* 1992). Seasonal ices are composed primarily of $CO_2$, with $H_2O$ and dust abundances probably reflecting their relative atmospheric abundances. The layered deposits, first observed in Mariner 9 images (see review by Thomas *et al.* 1992 and references therein), are well exposed in trough walls and at the cap margins. The layers appear to be approximately horizontal, to extend for tens of kilometers, and to be on the order of meters thick. Poorly known properties of the layered deposits relevant to assessing the magnitude of the load of the north polar cap on the martian lithosphere include the total volume of the layered deposits (their lateral extent and thickness beneath the residual polar ices are unknown) and their bulk composition, in particular the ice/sediment ratio. Although the layered deposits clearly reflect climatic effects, improved characterization of the layers would be necessary to establish links with climate cycles.

Investigations of how the mass anomaly associated with the polar cap is compensated require information on the gravity field. Pre-MGS spherical harmonic gravity field descriptions of Mars (Smith *et al.* 1993, Konopliv and Sjogren 1995) extend to degree and order 50 (wavelengths as short as 430 km), but the highest resolution is achieved only in a low-to-mid-latitude band. Resolution at high latitudes is substantially poorer. Malin (1986) estimated the density of the polar deposits to be $1 \pm 0.5$ kg m$^{-3}$ using line-of-site accelerations from seven Viking spacecraft orbits and a volume estimate for the polar cap derived from a reanalysis of the digital elevation model of Dzurisin and Blasius (1975). New high-resolution gravity (Smith *et al.* 1999) and topography data collected by the MGS spacecraft enable more confident analyses of compensation of polar cap topography.

Mars Orbiter Laser Altimeter (MOLA) elevation profiles obtained during a three-week period in fall 1997 and during the period March–September 1998 have yielded high-resolution topography for the northern polar cap and surrounding regions (Smith *et al.* 1998; Zuber *et al.* 1998a,b). The improved topography provides new insights into the relief and extent of previously defined geologic units. Here we summarize the topography and geologic setting of the polar cap and its environs. We employ elastic and viscoelastic models in order to investigate lithospheric loading and the consequent deflection of the underlying surface. We discuss the implications of lithosphere thickness for polar cap volume and heat flow into the base of the polar cap, and we explore time scales for relaxation of topography and the temporal evolution of the degree of compensation. Our modeling provides a context for investigations of modern cap dynamics and the influence of the cap on the moments of inertia and planetary dynamics of Mars. Finally we present evidence for a formerly larger northern polar cap and highlight such open issues as the time frame over which this larger cap may have persisted, the time scales for climate variations, the difficulties inherent to determining the past climate history, and the nature of interactions among climate history, cap evolution, and planetary dynamics.

## 2. PRESENT ICE CAP TOPOGRAPHY

MOLA data for the northern hemisphere, as of this writing, consist of 18 profiles from the aerobraking hiatus orbits (1997), 188 profiles from the science phasing orbits (1998) prior to (SPO-1) and following (SPO-2) Mars solar conjunction, and

more than 720 profiles collected during the the first two months of the ongoing mapping phase of the MGS mission. Because of the inclination of the MGS orbit, the generally nadir-pointing altimeter normally yields topographic measurements only southward of 86.3°N. Ten altimetry profiles were collected north of 86.3°N, however, by pointing the spacecraft approximately 50° off-nadir to enable the maximum height of the ice cap to be measured (Fig. 1a). Along-track resolution is 300–400 m, and the maximum vertical resolution is about 30 cm (Smith *et al.* 1998, Zuber *et al.* 1998b). Topography data presented in this paper are measurements of surface height relative to the geoid, which is computed from Mars gravity field model mgm0883 (Lemoine *et al.* 1999, Rowlands *et al.* 1999) and constrained to match the mean equatorial radius of $3396.0 \pm 0.3$ km (Zuber *et al.* 1998a).

The MOLA profile data have been used to construct a 2-km-resolution grid of the northern hemisphere topography for latitudes north of 55°N (Zuber *et al.* 1998b). Figure 1a shows a representation of the gridded topography northward of 60°N. The residual polar cap is asymmetric about the north pole, extending as far south as 78°N at longitudes near 0°E but extending southward only to 85°N in the region 140° to 220°E. However, if the dunes of Olympia Planitia (Fig. 1b) are underlain by residual ice, as suggested by Zuber *et al.* (1998b), then to first order the polar cap is symmetric about the north pole and has a radius of about 10° in latitude. Chasma Borealis, the largest reentrant (longitudes 330° to 10°E) into the polar cap, is clearly seen, and the MOLA data provide high-resolution profiles across many other chasmata and troughs. The surface of the ice cap is smooth on horizontal scales of less than a meter over baselines of hundreds of meters to kilometers and is smooth at the 10-m level over baselines of tens of kilometers (Zuber *et al.* 1998b). On average, the ice cap increases in height from its edge toward the pole. The highest point on the ice cap is at $-1950$ m $\pm$ 50 m and is within a few kilometers of the rotation pole.

Exterior to the ice cap the martian surface slopes downward toward the pole at all longitudes, with the greatest poleward slopes occurring over longitudes 220°–270°E at the northern periphery of the Tharsis Rise. The martian surface near the ice cap edge lies between $-4800$ m and $-5200$ m relative to the mean elevation of the equator. The relief of the ice cap is thus $2950 \pm 200$ m (Zuber *et al.* 1998b).

MOLA profiles across the region surrounding the residual cap provide additional important information on polar cap processes. Deposits immediately exterior to the residual cap have variable topographic signatures. In the longitude band 0°–60°E, the circumpolar plains deposits appear to be very smooth. In contrast, the plains deposits in the region 140°–255°E are interrupted by residual ice deposits (outliers, see below) of significant positive relief. Impact craters within 100 km of the permanent ice cap exhibit crater floor depths that are too shallow to be explained by impact-related structural uplift or interior wall collapse (J. B. Garvin, personal communication, 1999). The floors of several of these craters exhibit asymmetric topographic profiles. Both viscous relaxation and infilling of the crater cavities by ice or dust could account for the reduced relief. Asymmetric crater floor topography could result from viscous relaxation if lateral heterogeneities in rheology, related to changes in the depth and composition of the permafrost layer, are present.

## 3. GEOLOGIC SETTING

Geological mapping of the northern polar region has led to the indentification of several major units related to the present ice cap and possibly to an earlier, different cap geometry (Fig. 1b). The north polar cap and its circumpolar deposits are situated in the central part of the northern lowlands. Tanaka and Scott (1987) mapped the Hesperian-aged Vastitas Borealis Formation (Hv) over the majority of the northern lowlands. (A review of martian stratigraphy and associated nomenclature is provided by Tanaka *et al.* 1992.) On this older deposit are superposed the Amazonian-aged polar ice deposits (Api) and the closely associated polar layered deposits (Apl). The polar ice deposits correlate well with the topographic high of the present cap.

Surrounding the polar deposits in an annulus from approximately 70° to 80°N are circumpolar deposits of Amazonian age, including mantle material (Am) and two types of dune material, crescentic (Adc) and linear (Adl). Most of these deposits appear to be superposed on the Vastitas Borealis formation, obscuring or obliterating the topography characteristic of many of its members. Sources for the sediments composing the circumpolar units may include erosion of polar layered deposits, emplacement in association with some channel deposits, and eolian redistribution of regolith and other material. The thickness of the circumpolar deposits may vary substantially (Fishbaugh and Head 1999), forming thick units close to the polar cap and perhaps only a thin veneer at lower latitudes. Where the circumpolar deposits are thin, the regional slope will follow that of the underlying Vastitas Borealis formation. MOLA topography profiles extending across the Vastitas Borealis Formation northward toward the pole show breaks in slope in the latitude range 70°–78°N (Fig. 2, also Fishbaugh and Head 1999). The topography northward of the arrows indicated on each profile in Fig. 2, but southward of the polar deposits, is more nearly horizontal on average than topography southward of the arrow, which displays the regional poleward slope typical of the Vastitas Borealis Formation. Exceptions are in the area of the North Polar Basin (Head *et al.* 1998), where the topography is very flat and distinctive breaks in slope are less readily identified (Fig. 2, profiles from orbits 242 and 255). The break in slope appears to coincide with the margins of the circumpolar deposits mapped by Dial (1984) and Tanaka and Scott (1987) in the longitude region from 270° counterclockwise to 90°E (Fishbaugh and Head 1999, and profiles from orbits 255, 242, 210, and 252 in Fig. 2). The slope break does not correlate with the mapped Hesperian–Amazonian contact (Fig. 1b) in the longitude band 90°–270°E (Fig. 2, profiles from orbits 230, 224, and 256) but may reflect a change in thickness of the circumpolar deposits from thin,

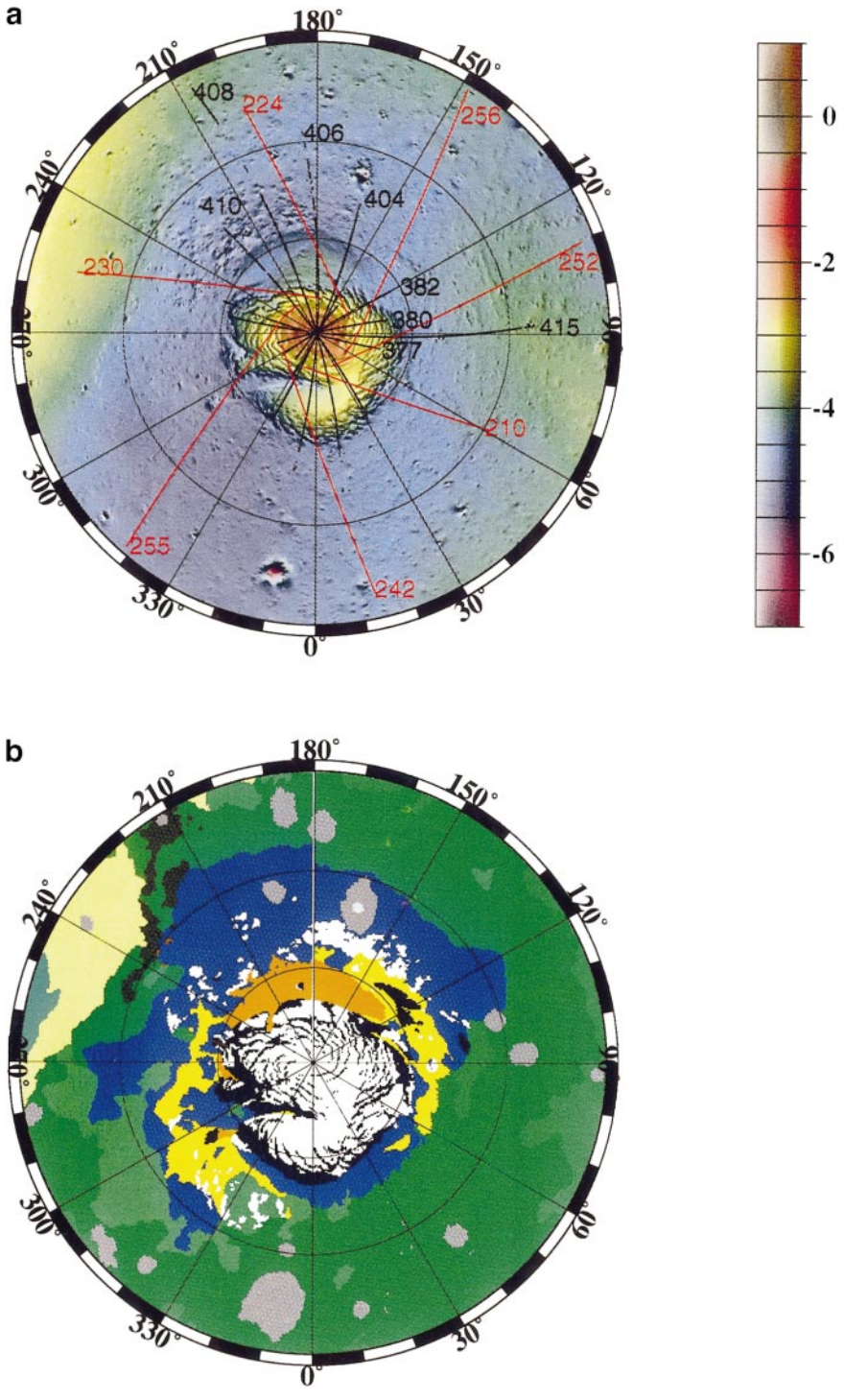


**FIG. 1.** (a) Gridded topography for the region 60°–90°N (Zuber *et al.* 1998b) obtained from MOLA data collected during the aerobraking hiatus and science phasing orbits. Color scale in kilometers is shown. MOLA orbit tracks marked in black indicate locations of off-nadir pole-crossing profiles shown in Fig. 4. MOLA orbit tracks marked in red indicate locations of profiles shown in Fig. 2. (b) Geologic map, simplified from Tanaka and Scott (1987). Units related to polar processes include: Api (white), residual polar deposits; Adl (orange), linear dunes; Apl (black), polar layered terrain; Am (blue), polar mantle material; Adc (dark yellow), crescentic dune material; Hv (green), subpolar plains deposits; and c (gray), cratered terrain. (b) also shows some units distant from the pole that are unrelated to polar processes. The lighter yellow and turquoise at longitudes 240°–270°E denote flows and sediments related to Alba Patera. A finger of ancient (Noachian) highland material (dark brown) is also seen at longitudes 210°–250°E.

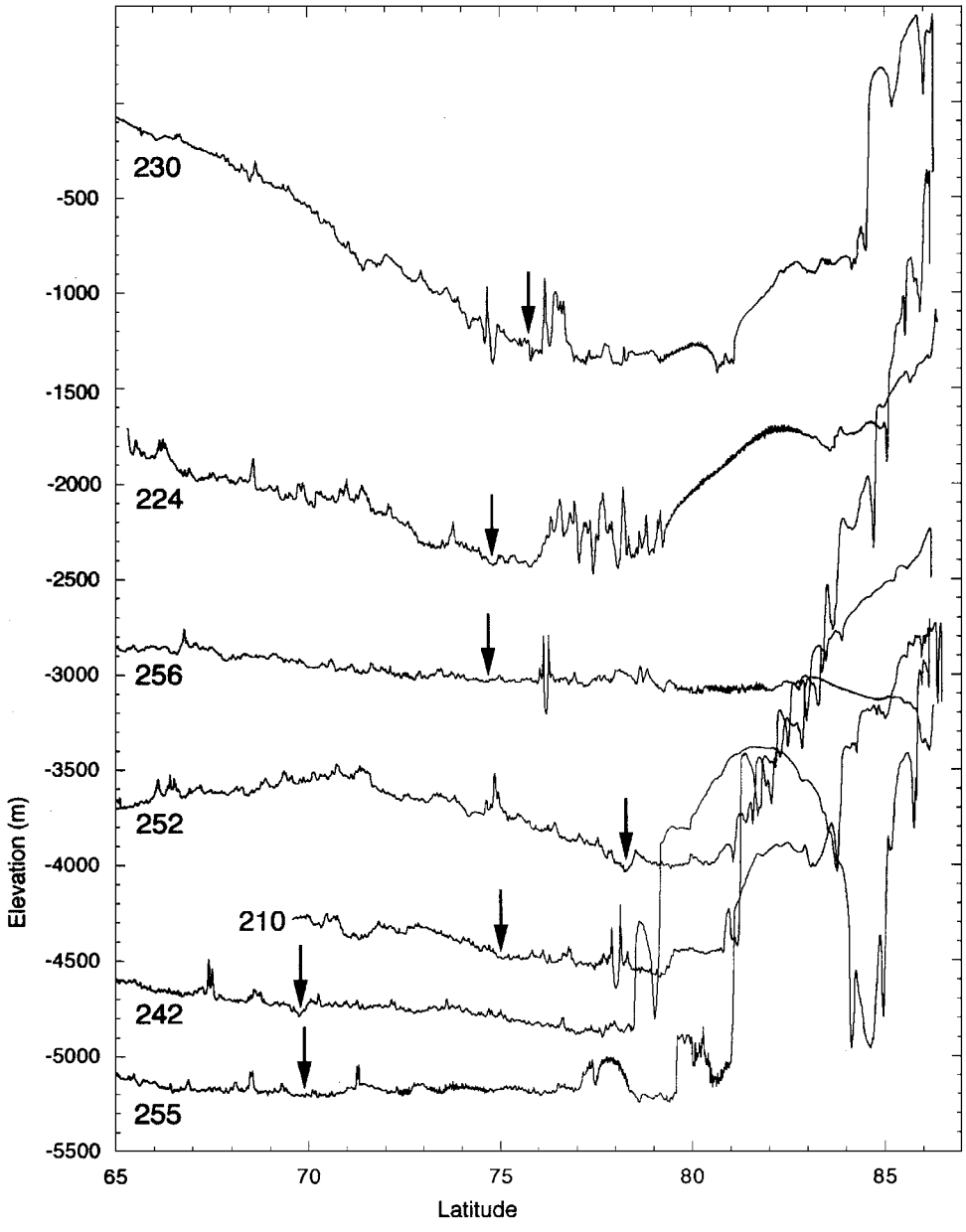


**FIG. 2.** MOLA topographic profiles for the ground tracks shown in red in Fig. 1a. Orbit numbers are given at the left of the profiles. Elevations shown for orbit 255 correspond to values indicated by the vertical axis; other profiles are offset vertically for clarity. Arrows indicate breaks in long-wavelength slope as identified by Fishbaugh and Head (1999).

mantling deposits southward of 75°N to thicker deposits northward of 75°N toward the polar cap. Circumpolar deposits may form thin veneers in other regions as well. For example, Zuber *et al.* (1998b) suggest that residual ice may underlie the linear dunes of Olympia Planitia on the basis of MOLA profile data across the dunes.

Outliers mapped as residual polar cap deposits are concentrated in a band from 70° to 80°N (Dial 1984, Tanaka and Scott 1987). MOLA data show that many of these outliers in the region from 140° to 255°E have significant relief (tens of meters to over 700 m relative to the surrounding regions), are tens of kilometers across (Fishbaugh and Head 1999), and have an albedo similar to that of the residual polar ices. The areal extent, relief, and albedo of the outliers suggest they are remnants of a formerly larger polar cap rather than seasonal features. This hypothesis is also supported by observations of topographic depressions (similar to terrestrial kettle holes related to glacier retreat) in the vicinity of the residual cap outliers (Fishbaugh and Head 1999). Residual polar cap material has been mapped in the cavities of some larger craters, such as in the crater centered at 73°N, 165°E (Tanaka and Scott 1987). The southerly latitudinal extent of the outliers correlates in general

with the locations of the break in slope identified in the profiles shown in Fig. 2. This correspondence suggests that the circumpolar deposits in the regions northward of the marked arrows in Fig. 2 could be derived, at least in part, from sediments once part of a formerly larger cap. While these observations are consistent with an increased cap size in the past, the spatial extent and timing of a larger polar cap are poorly constrained.

On the basis of impact crater densities, the polar materials (Api, Adl, Apl, Am, Adc) are inferred to be among the youngest deposits on the surface of Mars. The circumpolar deposits are clearly less heavily cratered than the underlying Hesperian-aged Vastitas Borealis formation. Although the polar layered deposits underlie the residual ice, their composite age is uncertain. While geologic mapping allows local stratigraphic relations to be established, the low impact crater densities on the polar units do not permit distinction among these units on the basis of average surface ages (Thomas *et al.* 1992).

## 4. ELASTIC LITHOSPHERIC LOADING MODELS

MOLA data provide high-resolution information on the topography of the upper surface of the polar cap. The degree to which the cap is compensated has implications for the depth to the basement underlying the cap and thus for the volume of the cap. We employ loading models for a thin spherical elastic shell as a means to investigate basement deflections and topographic signatures characteristic of flexural compensation of the cap. An outline of the model formulation is given in Section 4.1 below, and its application to the northern polar cap and assumptions invoked are described in Section 4.2.

### *4.1. Model Formulation*

The deflection $w$ due to an arbitrarily distributed load on a thin elastic lithospheric shell satisfies the differential equation

$$\left[D\nabla^6 + 4D\nabla^4 + 4D\nabla^2 + ET_eR^2\nabla^2 + 2ET_eR^2\right]w = R^4(\nabla^2 + 1 - \nu)q \quad (1)$$

(Kraus 1967, Willemann and Turcotte 1981). $D = ET_e^3/12(1-\nu^2)$ is the flexural rigidity, where $T_e$ is the elastic shell thickness, $E$ is Young's modulus, $\nu$ is Poisson's ratio, $R$ is the mean radius of the shell ($R = R_p - T_e/2$, where $R_p$ is the planetary radius), and $q$ is the effective local normal stress on the shell. $\nabla^2$ is the Laplacian operator defined in a spherical coordinate system and evaluated at the mean radius of the shell, and $w$ is positive radially outward. Contributions to $q$ (positive outward) come from the applied load corresponding to the original ice cap topography and from the restoring force due to the density contrast at the depressed crust–mantle boundary beneath the load. In this formulation shear stresses are assumed to be insignificant in magnitude in comparison with normal stresses. As we are primarily interested in the long-wavelength deflection of the subice basement this is a reasonable assumption (Banerdt 1986). We shall see later that gravity field predictions from a model that includes shear stresses (Banerdt 1986, Phillips *et al.* 1999) are very similar to those predicted using the formulation described above. For loads with a wavelength on the order of the planetary radius, there is an additional term due to the (upward) displacement of the geoid and so

$$q = -(\rho_{ice}gh - \rho_m g h_g - \Delta\rho g w), \quad (2)$$

where $g$ is the gravitational acceleration, $\rho_m$ and $\Delta\rho$ are the mantle density and the density contrast responsible for the restoring normal stresses, respectively, $\rho_{ice}$ is the load density, $h$ is the topography of the load, and $h_g$ is the deflection of the geoid resulting from the additional mass of the topography. Substituting (2) into (1) gives

$$\left[D\nabla^6 + 4D\nabla^4 + 4D\nabla^2 + ET_eR^2\nabla^2 + 2ET_eR^2 - \Delta\rho g(\nabla^2 + 1 - \nu)\right]w = -\rho_{ice}g(\nabla^2 + 1 - \nu)\bar{h}, \quad (3)$$

where $\bar{h}$ is the modified load given by $h - (\rho_m/\rho_{ice})h_g$. Assuming no flexural moat infill or cap flow, $\Delta\rho = \rho_m$. For loads of a wavelength small compared with the planetary radius, $\bar{h} \approx h$.

This formulation includes both membrane and bending stresses. For loads having a wavelength small compared with $R$, (3) reduces to a simpler form [see, e.g., Eq. (1) of Brotchie and Sylvester (1969) and Eq. (5) of Turcotte *et al.* (1981)]. The present lateral extent of the northern polar cap on Mars is significant and, as discussed above, may have been greater in the past, so we solve (3) explicitly.

As in Turcotte *et al.* (1981) we introduce the dimensionless parameters $\tau$ and $\sigma$ given by

$$\tau = \frac{ET_e}{R^2 g \Delta\rho} \quad (4)$$

and

$$\sigma = \frac{D}{R^4 g \Delta\rho}. \quad (5)$$

$\tau$ is a measure of the rigidity of the spherical shell if bending resistance is neglected, and $\sigma$ is a measure of the resistance of the shell to bending. The topography of the load $h$, the modified load $\bar{h}$, the displacement of the geoid $h_g$, and the resulting deflection $w$ can be expressed as spherical harmonic expansions

$$h(\theta,\phi) = R_p \sum_{l=2}^{\infty}\sum_{m=0}^{l} P_l^m(\cos\theta)\left(C_l^m \cos m\phi + D_l^m \sin m\phi\right) \quad (6)$$

$$\bar{h}(\theta,\phi) = R_p \sum_{l=2}^{\infty}\sum_{m=0}^{l} P_l^m(\cos\theta)\left(\bar{C}_l^m \cos m\phi + \bar{D}_l^m \sin m\phi\right) \quad (7)$$

$$h_g(\theta,\phi) = R_p \sum_{l=2}^{\infty}\sum_{m=0}^{l} P_l^m(\cos\theta)\left(C_{gl}^m \cos m\phi + D_{gl}^m \sin m\phi\right) \quad (8)$$

$$w(\theta,\phi) = R_p \sum_{l=2}^{\infty}\sum_{m=0}^{l} P_l^m(\cos\theta)\left(A_l^m \cos m\phi + B_l^m \sin m\phi\right) \quad (9)$$

where $\theta$ and $\phi$ are colatitude and longitude, respectively, $P_l^m$ are the associated Legendre polynomials of degree $l$ and order $m$, and the coefficients of the sine and cosine terms are constants satisfying full normalization of each spherical harmonic. Substituting (4), (5), (7), and (9) into (3) and solving (3) in the spectral domain yields the relationship

$$\begin{pmatrix} A_l^m \\ B_l^m \end{pmatrix} = -\frac{\rho_{ice}}{\Delta\rho}\alpha_l \begin{pmatrix} \bar{C}_l^m \\ \bar{D}_l^m \end{pmatrix}, \quad (10)$$

where $\alpha_l$ is given by

$$\alpha_l = \frac{-[l(l+1)-(1-\nu)]}{\sigma[-l^3(l+1)^3+4l^2(l+1)^2-4l(l+1)]+\tau[-l(l+1)+2]+[-l(l+1)+(1-\nu)]}. \quad (11)$$

The spherical harmonic coefficients in the expansions of $h_g$, $h$, and $w$ are related by

$$\begin{pmatrix} C_{gl}^m \\ C_{gl}^m \end{pmatrix} = \frac{3}{(2l+1)\bar{\rho}}\left[\rho_{ice}\begin{pmatrix} C_l^m \\ D_l^m \end{pmatrix} - \Delta\rho\begin{pmatrix} A_l^m \\ B_l^m \end{pmatrix}\right], \quad (12)$$

where $\bar{\rho}$ is the mean density of the planet. Thus

$$\begin{pmatrix} A_l^m \\ B_l^m \end{pmatrix} = -\frac{\rho_{ice}}{\Delta\rho}\gamma_l \begin{pmatrix} C_l^m \\ D_l^m \end{pmatrix} \quad (13)$$

with

$$\gamma_l = \left[1 - \frac{3\rho_m}{(2l+1)\bar{\rho}}\right]\left[\frac{1}{\alpha_l} - \frac{3\rho_m}{(2l+1)\bar{\rho}}\right]^{-1}. \quad (14)$$

$(A_l^m, B_l^m)$ and $(C_l^m, D_l^m)$ are the fully normalized coefficients of the spherical harmonic expansions of the topography $h$ and deflection $w$, respectively. For loads of wavelengths much less than $R$, $\alpha_l \approx \gamma_l$.

The elastic response of the lithosphere to an arbitrary topographic load $h$ can be modeled by expanding the load in spherical harmonics and computing $\alpha_l$, $\gamma_l$, and hence $w$ from Eqs. (6)–(14). The resulting topography $h'$ is given by $h' = h + w$.

Finally, this approach can also be used to compute the gravity anomaly over the polar cap. We assume a single crustal layer of thickness $T_c$. If the gravity field is expressed as a spherical harmonic expansion

$$\Delta g(\theta,\phi) = R_p \sum_{l=2}^{\infty}\sum_{m=0}^{l} P_l^m(\cos\theta)\left(S_l^m \cos m\phi + T_l^m \sin m\phi\right) \quad (15)$$

then the spherical harmonic coefficients $(S_l^m, T_l^m)$ are given by

$$\begin{pmatrix} S_l^m \\ T_l^m \end{pmatrix} = -4\pi G\rho_{ice}\left(\frac{l+1}{2l+1}\right)\left[1-\left(1-\frac{T_c}{R_p}\right)^{l+2}\gamma_l\right]\begin{pmatrix} C_l^m \\ D_l^m \end{pmatrix}, \quad (16)$$

where $G$ is the gravitational constant.

### 4.2. Polar Ice Cap Loading

On the basis of the above formulation we examine loading of the martian lithosphere by the northern polar cap. We assume that the surface on which the ice rests would, in the absence of the polar cap, be perfectly spherical. Exterior to the cap the long-wavelength topography of the northern polar region indicates that the ice cap lies off-center in a broad, shallow-relief saddle (superposed on the spherical planetary surface). This shallow-relief saddle may result in long-wavelength deviations of up to 200 m of the underlying original (i.e., unloaded) surface from a spherical surface; we examine the implications of such deviations from sphericity for the estimates of polar cap volume below. The topography surrounding the northern polar cap is extremely smooth at large and small scales (Smith *et al.* 1998). While it is impossible to rule out undetectable topographic features beneath the polar cap, the long- and short-wavelength features of the topography surrounding the cap suggest a smooth original surface of low relief.

Key parameters adopted in our modeling are given in Table I. In the absence of strong constraints on the density of the polar ice cap, we use a nominal value of 1000 kg m$^{-3}$, a figure that neglects the presence of dust, sediments, and volatiles other than water. Predicted lithospheric deflections scale linearly with ice cap density, however, so we also examine the implications of this assumption for such inferences as ice cap volume. A more complex issue is that of the temporal evolution of the ice cap, both the gross changes in height and extent of the cap and the time scales over which such changes have occurred. Initially we

**TABLE I**
**Parameter Values for Flexural Loading Models**

| Parameter | Value |
|---|---|
| Young's modulus, E | $10^{11}$ N m$^{-2}$ |
| Poisson's ratio, $\nu$ | 0.25 |
| Mean density, $\bar{\rho}$ | 3940 kg m$^{-3}$ |
| Mantle density, $\rho_m$ | 3500 kg m$^{-3}$ |
| Load density, $\rho_{ice}$ | 1000 kg m$^{-3}$ |
| Gravitational acceleration, $g$ | 3.72 m s$^{-2}$ |
| Planetary radius, $R_p$ | 3397 km |

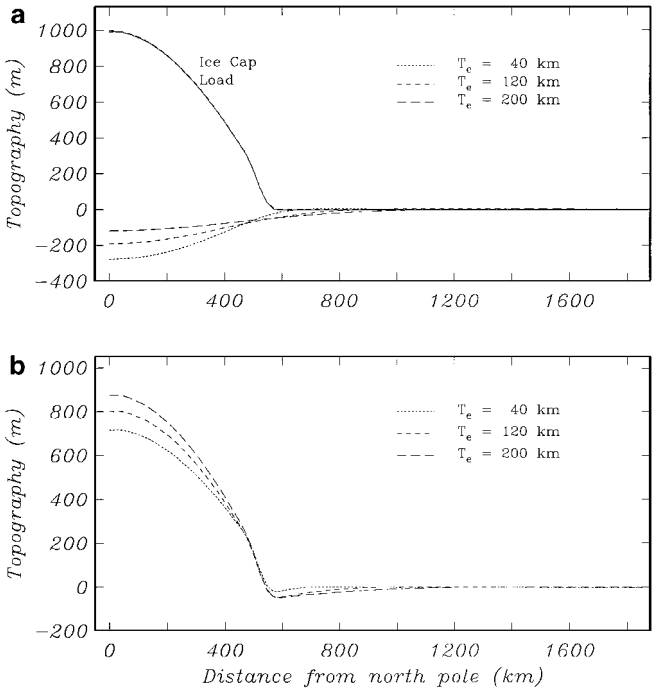


**FIG. 3.** (a) Upper profiles depict the topography of the model ice cap load; the dashed line shows the analytical expression for the load (a cosine of colatitude with quarter wavelength of 593 km and maximum amplitude 1 km), while the solid line is the load reconstructed from its spherical harmonic expansion. Lower profiles show the deflection of the original surface, as a function of elastic shell thickness, for the model. (b) Final topography for the elastic shell thicknesses in (a).

investigate a simplified scenario, examining the response of an elastic lithosphere over an inviscid interior to a load of extent and relief similar to those of the present cap.

The 10 off-nadir MOLA profiles across the polar cap indicate that the cap shape can be approximated to first order by a simple axisymmetric function, which we take to be the first quarter cycle of a cosine of colatitude. The spherical harmonic expansion of this simplified load is calculated and the deflection $w$ and final topography $h'$ computed for a range of values for the effective elastic lithosphere thickness. Sample forward models are shown in Fig. 3 for a unit ice cap relief (1 km), a quarter wavelength of 593 km (corresponding to a polar cap radius of 10° in latitude), and effective elastic thicknesses $T_e$ of 40, 120, and 200 km. The change in slope of the load topography at a distance of approximately 500 km is due to tapering of the load edge to avoid numerical problems. The lithospheric deflection scales linearly with the peak applied (or final) load and with the ice cap density. We scale the predicted final topography $h'$ to match the relief of the present ice cap of $2950 \pm 200$ m (Zuber *et al.* 1998b) (Figs. 4 and 5). The 10 off-nadir MOLA profiles across the polar cap are compared with the final topography predicted from our simplified load geometry in Fig. 4. The MOLA profiles show the clear symmetry of the polar cap topography about the rotation pole for latitudes above 85°N (distances of 0–300 km). An excellent match of the model profiles to the MOLA data is seen for three orbits (377, 380, and 415) that cross topographically symmetric regions of the cap. The model provides a good average fit to orbits (404, 406, 408, and 410) that cross the cap over Olympia Planitia and the Chasma Borealis regions, features which are clearly asymmetric about the rotation axis. The model overestimates the height of the cap for two orbits yielding rather short profiles (384 and 385) and for orbit 382.

Basement deflections for the isostatic case ($T_e = 0$ km) and for effective elastic lithosphere thicknesses of 40, 80, 120, 160, and 200 km are shown in Fig. 5. For this range of elastic thicknesses and a cap density of 1000 kg m$^{-3}$, the base of the northern polar cap could extend from 400 to 1180 m below the level of the cap edge. The total mass of dust and sediments in the polar cap load is unknown, but reasonable lower and upper bounds on the cap density are 1000 and 2000 kg m$^{-3}$, respectively. Because the basement deflection scales linearly with the load density, the base of the polar cap could lie more than 2 km below the level of the cap edge for a cap load of density 2000 kg m$^{-3}$ supported by a thin elastic lithosphere. There is little evidence for a discernible outer-rise signature in the model-predicted topography exterior to the ice cap, a result attributed to the distributed nature of the load and to partial support of the load by membrane, rather than flexural, stresses. The extent and depth of the predicted flexural moat varies with elastic thickness.

### *4.3. Gravity Field Predictions*

Identification of the degree to which the polar cap is compensated requires information on the gravity field. The gravity field arising from a (known) topographic load and its flexural compensation can be computed using Eq. (16). Figure 6 shows the results of such a calculation using our axisymmetric load model for a range of elastic plate thicknesses $T_e$ of 40–200 km and for crustal thicknesses $T_c$ of 10 and 50 km, selected as illustrative values. Also shown is the gravity anomaly that would be produced by uncompensated topography (solid line). As expected, there is a trade-off between $T_c$ and $T_e$, particularly for $T_e$ less than about 100 km. The peak gravity anomaly due to uncompensated topography is 129 mGal. Flexural compensation of topography could result in a relative gravity low of about −20 mGal close to the edge of the polar cap.

The gravity anomaly predicted using a more detailed representation of the topography field and a model for loading of a thin elastic shell that includes tangential stresses (Banerdt 1986) is shown in Fig. 7. A total crustal thickness $T_c$ of 50 km, an elastic thickness $T_e$ of 120 km, a load density of 1500 kg m$^{-3}$, and a value for the Young's modulus of $10^{11}$ Nm$^{-2}$ were assumed. When considering the difference in model load densities, overall good agreement is seen between the gravity field predicted from this model (Fig. 7) and that predicted from our simplified model (Fig. 6) for the appropriate choices of $T_e$ and $T_c$. Figure 7 also shows a recent gravity field model for Mars (Smith *et al.* 1999); both the gravity field model ("observed gravity") and the elastic shell model were expanded from spherical harmonic degrees 2

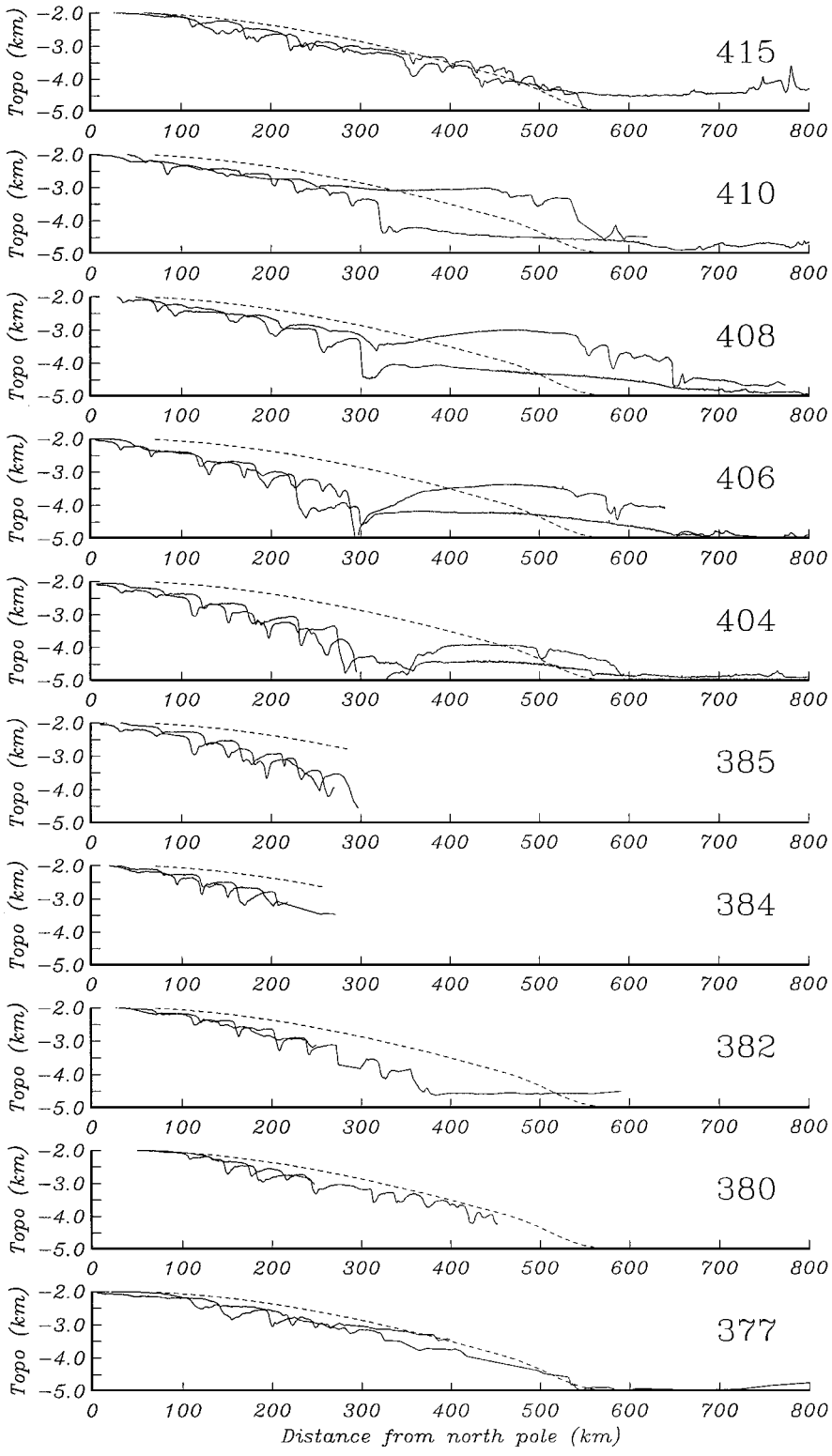


**FIG. 4.** Off-nadir profiles (solid) crossing the polar cap, plotted as a function of distance from the north pole. Ground tracks for these orbits are shown in Fig. 1a. Dashed lines are the predicted final topography generated by assuming a cosine load and matching the final relief to the value of 2950 m of Zuber *et al.* (1998b). The model profiles have been shifted by −5 km to match the MOLA data.

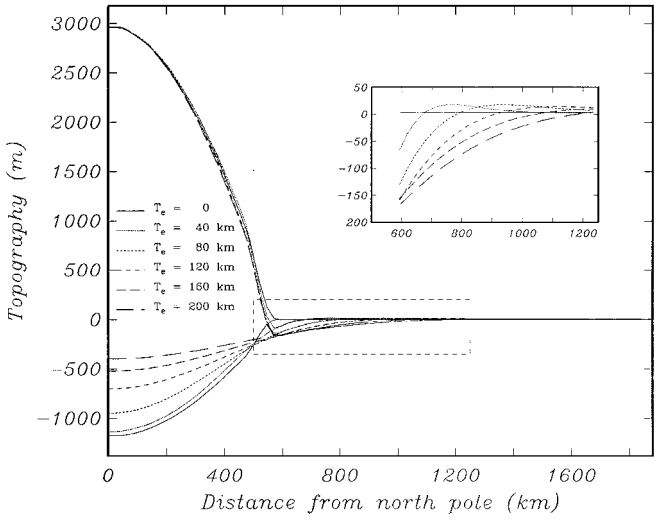


**FIG. 5.** Model ice cap relief and basement deflection, scaled such that the ice cap relief matches the 2950 m value given by Zuber *et al.* (1998b). Region outlined by the dashed box is magnified in the inset to show predicted deflections in the vicinity of the ice cap edge.

to 52 (employing a cosine taper from degrees 48 to 52). The agreement between the observed and modeled field is good over the western hemisphere portion of the main cap between about 85°N and the pole, but gravity anomalies over the cap southward of 85°N and circumcap anomalies are not reproduced by the topographically loaded flexure model.

## 5. VISCOELASTIC LOADING MODELS

The models described above are based on the response to an applied load of an elastic lithosphere over an inviscid substrate. Particularly for long-wavelength loads, such as the northern polar cap, it is important to examine the viscous relaxation time of topography and its relationship to the temporal evolution of the load. Here we investigate the viscoelastic response of a spherical planet to a temporally invariant load of wavelength $\lambda$. The response is described by the governing equations of mass and momentum conservation and the equation of gravitational perturbation

$$u_{i,i} = 0 \tag{17}$$

$$\sigma_{ij,j} + \rho(r)\phi_{,i} - \Delta\rho g\delta_{ij} = 0 \tag{18}$$

$$\phi_{,ii} = 4\pi G\Delta\rho, \tag{19}$$

where $u_i$ is velocity, $\sigma_{ij}$ is stress, $\rho(r)$ is density, $\phi$ is the perturbation of the gravitational potential, $g$ is the gravitational acceleration, $\Delta\rho$ is the density pertubation associated with the load, and summation over repeated indices is implied. The rheology of an incompressible Maxwell viscoelastic medium is given by

$$\sigma_{ij} + (\eta/\mu)\,\sigma_{ij,t} = -P\delta_{ij} + 2\eta\epsilon_{ij,t}, \tag{20}$$

where $\eta$ and $\mu$ are viscosity and shear modulus respectively, $P$ is pressure, and $\sigma_{ij,t}$ and $\epsilon_{ij,t}$ are the time derivatives of stress and strain, respectively.

For a specified load and set of planetary mechanical properties, an analytical solution for the time evolution of stresses and surface deflections can be obtained (Zhong and Zuber 2000). The adopted model parameters are given in Table II. (Note that the parameters of the planetary core are unimportant, as the solution for loads of wavelengths relevant to this problem is insensitive to deep structure.) Loads of full wavelength comparable to and

**TABLE II**
**Parameter Values for Viscoelastic Loading Models**

| Parameter | Value |
|---|---|
| Planetary radius, $R_p$ | 3400 km |
| Crustal thickness, $T_c$ | 50 km |
| Nominal elastic shell viscosity | $10^{30}$ Pa-s |
| Nominal mantle viscosity | $10^{21}$ Pa-s |
| Shear modulus | $10^{11}$ Pa |
| Crustal density, $\rho_c$ | 2800 kg m$^{-3}$ |
| Mantle density, $\rho_m$ | 3500 kg m$^{-3}$ |
| Core density, $\rho_{co}$ | 6600 kg m$^{-3}$ |
| Core radius, $R_{co}$ | 0.5 $R_p$ |

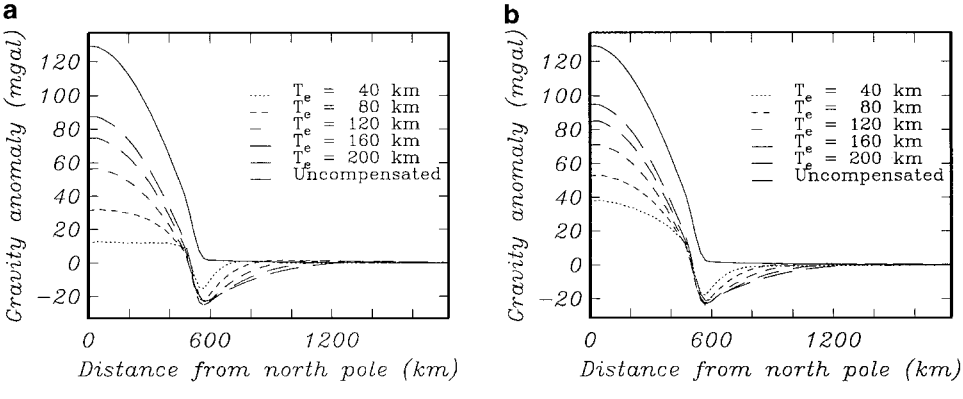


**FIG. 6.** Free-air gravity anomaly at $r = R_p$ predicted by the axisymmetric cosine load for the elastic thicknesses in Fig. 4. The solid line shows the expected gravity anomaly for uncompensated topography. The predicted gravity anomalies for crustal thicknesses of 10 and 50 km are shown in (a) and (b), respectively.

smaller than twice the cap diameter (or spherical harmonic degrees 9 and greater) have been investigated.

The relaxation of loads of degree 9, 18, and 36 as a function of time is shown in Fig. 8 for effective elastic thicknesses of 0, 50, and 100 km. Relaxation in Fig. 8 is represented by the degree of compensation (Turcotte *et al.* 1981), defined as the ratio of the observed deflection to that which would occur if a lithosphere having no strength were subjected to the same load. Several important inferences can be made from the figure. First, for all values of effective elastic lithosphere thickness shown, a portion of the load relaxes over a characteristic time given by the Maxwell time $\tau_m$. For an upper mantle viscosity of $10^{21}$ Pa-s, a value similar to that of the Earth's upper mantle, the Maxwell time is $10^5$ yr. If the mantle viscosity were as great as $10^{23}$ Pa-s, the Maxwell time would be $10^7$ yr (Zhong and Zuber 2000). Second, for models incorporating an elastic lithosphere, the shortest wavelengths remain uncompensated, even over time scales of $10^8$ yr. Third, for a given wavelength load, there is an asymptotic limit to the compensation state that is controlled by the effective elastic lithosphere thickness $T_e$. For longer wavelength loads, substantial variation in the asymptotic limit is seen for $T_e$ in the range 0–100 km.

## 6. DISCUSSION

The flexural and viscoelastic lithospheric loading models presented here provide bounds on the volume of the present northern polar cap (under the assumptions specified at the beginning of Section 4.2) and predictions for the degree of compensation of polar cap topography given specific lithospheric properties. However, even with detailed information on the current gravity and topography over the polar region, inferences on compensation mechanism and thus of lithospheric structure require knowledge of the temporal evolution of the polar cap. If the polar cap mass and spatial extent have changed significantly over time scales comparable to the Maxwell time $\tau_m$, the present gravity and topography will reflect not only the present cap geometry but the time-integrated history of the cap.

### *6.1. Present Cap Geometry: Implications for Lithospheric Loading*

We first discuss the implications of our lithospheric loading models under the premise that the present cap geometry has persisted over a time period longer than $\tau_m$ ($10^5$ yr for a mantle viscosity of $10^{21}$ Pa-s). For this assumption to hold, the time scales associated with processes causing significant changes in the mass and extent of the cap, including cap dynamics and climate variations, operate over time scales longer than $\tau_m$. Under these conditions, the present cap is in quasi-steady state (relative to $\tau_m$) and the models described above provide some insight into compensation of cap topography.

The elastic plate calculations of Section 4.2 show that the volume of the northern polar cap depends strongly on the effective elastic lithosphere thickness and on the average density of the load. Using a lower bound on mean cap density, that of $H_2O$ ice (1000 kg m$^{-3}$), our axisymmetric cap model gives volume estimates for the cap that vary by 43% for uncompensated to fully compensated topography. For effective elastic lithosphere thicknesses in the range 200 to 40 km, the volume calculated from our axisymmetric cap model lies in the range 1.5 to $1.8 \times 10^6$ km$^3$. Because of the unknown ice/sediment ratio in the cap, the average cap density is uncertain to within about a factor of two. A plausible upper bound on mean cap density of 2000 kg m$^3$ corresponds to volume estimates for our axisymmetric cap model that lie in the range 1.8 to $2.3 \times 10^6$ km$^3$. Earlier we noted that the long-wavelength topography surrounding the northern polar cap is consistent with the premise that the cap lies on a broad, low-relief saddle. Given that the variation in mean elevation surrounding the cap is $\pm$200 m, we conservatively assume an uncertainty in the depth to basement of 200 m everywhere beneath the cap. This assumption yields an uncertainty in the cap volume of $0.6 \times 10^6$ km$^3$.

Lithospheric thickness in the northern polar region not only affects the subsidence beneath the cap but also constrains the heat flow into the base of the ice cap. A thin lithosphere implies high values for lithospheric thermal gradient, heat flow, and basement subsidence, while a thick lithosphere implies low values for these quantities. For a given lithosphere thickness the maximum temperature at the base of the polar cap can be calculated, as the thickness of the polar cap follows from elastic shell calculations (Fig. 4). We assume that the base of the elastic lithosphere corresponds to the 550°C isotherm and use an average Earth-like value for the thermal conductivity of the lithosphere of 3.3 W m$^{-1}$ K$^{-1}$ (McNutt 1984). A value of 160 K (Squyres *et al.* 1992) is used for the annual mean surface temperature at the pole, and the thermal conductivity of ice at this temperature is 3.8 W m$^{-1}$ K$^{-1}$ (Fletcher 1970). For the following calculations we use the basement deflections shown in Fig. 4 for a pure $H_2O$-ice cap. For a 200 km-thick lithosphere, thermal gradients are low and the temperature at the base of the polar cap is 170 K, a value close to the mean surface temperature. In contrast, a 40-km-thick lithosphere results in high thermal gradients and temperatures of up to 215 K at the base of the polar cap. The presence of sediments in the polar cap will increase the cap density and cause greater subsidence beneath the cap, thus increasing the predicted temperature at the base of the cap. The thermal conductivity of the cap will also decrease somewhat, further increasing the basal temperature. If the cap density is increased to 2000 kg m$^{-3}$ and the thermal conductivity decreased to 3.5 W m$^{-1}$ K$^{-1}$ (values intermediate between the thermal conductivities for ice and rock specified above), the temperature at the base of the polar cap would be 234 K for a 40-km-thick lithosphere. The pressure dependence of the melting point of $H_2O$ ice is minor ($-7.4 \times 10^{-8}$ K Pa$^{-1}$, Hobbs 1974), and the melting point at the base of even a thick cap is reduced by only a few degrees relative to that at the surface. Dissolved salts within the ice cap, however, could reduce the melting point sufficiently that for a thin lithosphere the temperature at the base of the cap may approach the melting point of the mixture.

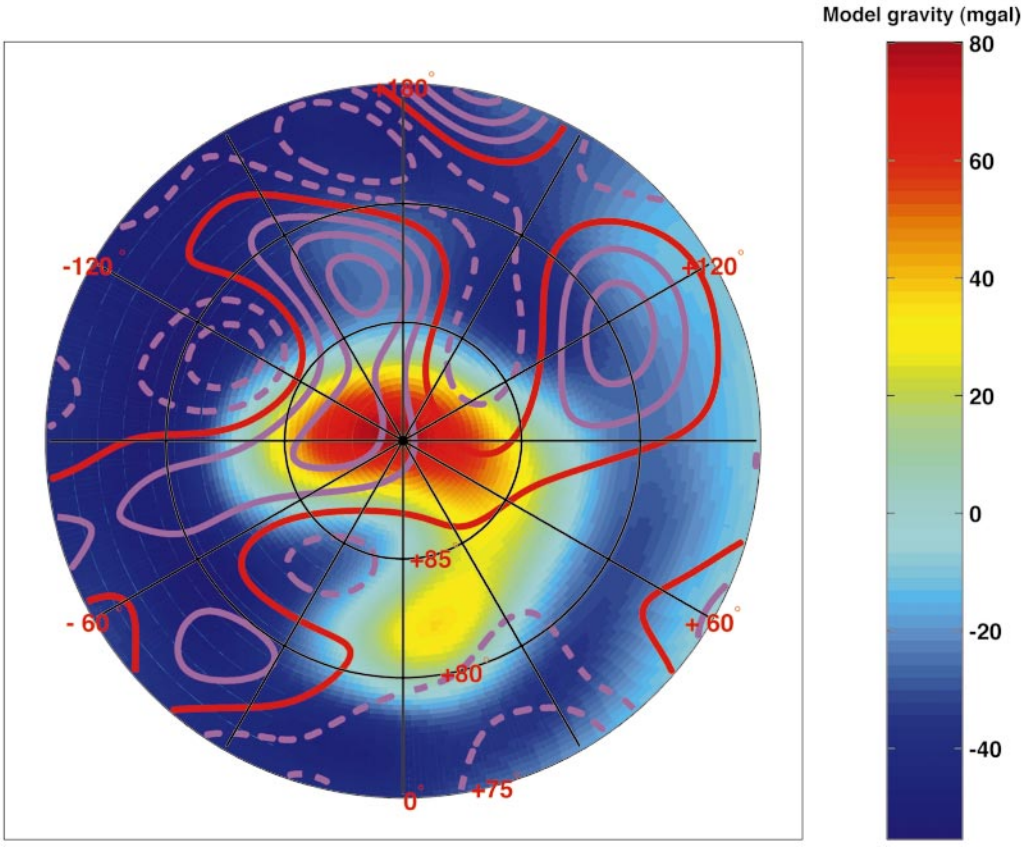


**FIG. 7.** Free-air gravity anomaly at $r = R_p$ predicted using the spherical elastic shell flexure model of Banerdt (1986) and a band-limited spherical harmonic expansion of MOLA-derived gridded topography (Zuber *et al.* 1998b). Elastic lithosphere thickness is 120 km, crustal thickness is 50 km, and load, crust, and mantle densities are 1500, 2900, and 3300 kg $m^{-3}$, respectively (see text for details). Color-shaded image shows the model-derived gravity field. Contours show a similarly bandpass-filtered Mars gravity field model (Smith *et al.* 1999). Solid contours are positive anomalies, dashed contours are negative anomalies, the zero contour is shown in red, and the contour interval is 50 mGal.

The inferred temperatures at the base of the polar cap clearly have implications for the rheology of the ice and thus for viscous flow of the cap. Models in which viscous flow balances accumulation produce a best fit to polar cap topography for outward flow velocities of less than 1 mm per martian year, assuming a rheology appropriate to $H_2O$ ice and a temperature for the cap material governed by the mean annual surface temperature in the northern polar region (Zuber *et al.* 1998b). The above discussion shows that vertical temperature gradients in the polar cap may be significant, with enhanced temperatures at the base of the cap leading to greater basal flow and shear stresses within the cap (Hooke 1998). The maximum relief of the polar cap may thus be controlled by basal flow.

MOLA data alone provide little information on effective elastic lithosphere thickness because topography exterior to the polar cap is dominated by long-wavelength features unassociated with polar processes that mask any consistent flexural moat–outer rise signature. However, MOLA data in conjunction with geologic mapping may provide tentative constraints on $T_e$. One interpretation for the break in slope identified in the profiles shown in Fig. 2 is that it corresponds to the boundary between the northward-sloping Hesperian units and the Amazonian-age circumpolar deposits that fill a flexural topographic depression immediately outward of the cap. In some regions (e.g., longitudes 135° to 270°E) the older Hesperian units may be covered with a mantle of Amazonian-age deposits too thin to modify the regional slope imparted by the underlying Hesperian units. Such a relationship would account for the lack of correlation of the mapped contact between the Amazonian and Hesperian units with the break in slope indentified in Fig. 2 within this longitude band. By this interpretation, the flexural moat would have a southerly latitudinal limit of 75° to 78°N, or 120 to 300 km from the edge of the polar cap. (For the purposes of this discussion we ignore profiles that cross the North Polar Basin, for which the identified location of the break in slope is less robust.) The flexural profiles in Fig. 5 indicate that a flexural moat of width 120–300 km could be generated by the response of a 60–120 km thick elastic lithosphere to the cap load.

As noted earlier, the breaks in slope identified in Fig. 2 also correlate with the southerly limit of polar cap outliers. The sediments north of the identified slope breaks could therefore reflect sediments deposited from a retreating former cap of larger

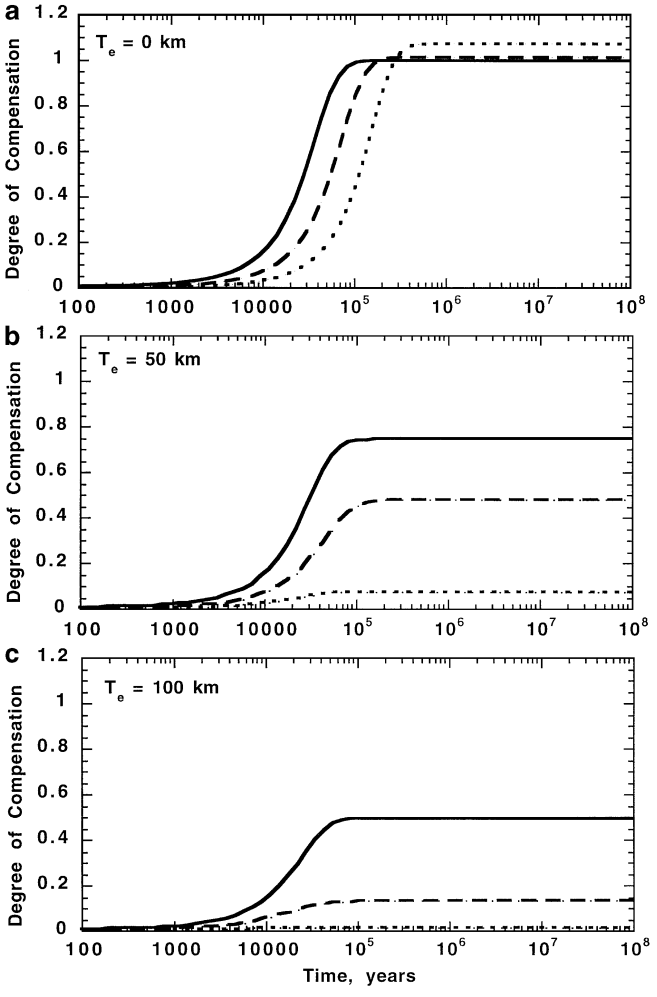


**FIG. 8.** Degree of compensation for loads of varying wavelengths and an elastic lithosphere of thickness (a) 0 km, (b) 50 km, and (c) 100 km. Solid, dashed, and dotted lines correspond to loads of degree 9 (twice the polar cap diameter), 18, and 36. The calculations assume a crustal thickness of 50 km and a mantle viscosity of $10^{21}$ Pa-s; the latter results in a relaxation time for the loads of $10^5$ yr. The slight overcompensation for the degree 36 load on a strengthless lithosphere occurs because of the influence of the crust–mantle boundary on the stress state. In this case local isostasy is not the asymptotic limit of the lithospheric response to loading (Zhong 1997).

lateral extent than the present cap. The breaks in slope identified in Fig. 2 and the polar cap outliers would then both be consistent with an earlier cap extending southward to at least approximately 75°N over a significant longitudinal range. By this reasoning, the circumpolar depression filled by Amazonian sediments would be related to the extent of the formerly larger cap, rather than to the flexural response of the lithosphere to the present cap, prohibiting inferences on effective elastic lithosphere thickness.

Modeling of the free-air gravity anomaly associated with the polar cap topography and comparisons with current gravity field models indicate that interpretation of gravity anomalies in the northern polar region is a difficult problem. The modeling described in Section 4.3 suggests that the broad gravity high over the central part of the polar cap may reflect flexural compensation of topography. Values for effective elastic lithosphere thickness and crustal thickness of 120 and 50 km, respectively, are consistent with current gravity fields over the western hemisphere portion of the main cap for a cap density of 1500 kg $m^{-3}$ (Fig. 7), although of course these values are nonunique. Lower values of $T_e$, consistent with the range inferred on the basis of geology and meridional slope above, would provide a similar fit to the gravity field for higher load densities (Eq. 16).

The poor correlation of gravity anomalies and topography over much of the north polar region is puzzling. If the long-wavelength gravity anomaly associated with the whole of the cap (80°N to the pole at most longitudes) is examined, then the observation that much of the polar cap has no associated gravity high would lead to an interpretation favoring significant compensation of the long-wavelength polar cap load, through viscous relaxation and/or a thin effective elastic lithosphere thickness. The inference that the longest wavelengths associated with the cap have at least partially relaxed is supported by the viscoelastic calculations shown in Fig. 8, as long as the cap is at least as old as the Maxwell time. Under the alternative interpretation, i.e., that the main part of the polar cap is reflected in the gravity signal, the shorter wavelength anomalies, uncorrelated with topography, may reflect a combination of such effects as laterally varying crustal and lithospheric properties (e.g., lateral variations in upper crustal density related to variable ice/sediment ratios, Phillips *et al.* 1999) and spatial variations in the degree of compensation due to the removal and deposition of material at different spatial scales.

### *6.2. Temporal Evolution of the Polar Cap: Implications for Lithospheric Loading*

The above discussion on polar cap volume and basal temperatures and inferred thicknesses of the effective elastic lithosphere was based on the assumption that the present cap geometry has persisted over time scales longer than the Maxwell time for the martian mantle. The temporal evolution of the polar cap is, of course, closely coupled to the climate history of Mars. Climate history is in turn strongly affected by quasi-periodic variations in planetary obliquity (the angle between the spin axis and the normal to the orbit plane of Mars), which cause changes in the average insolation as a function of latitude. These changes lead to an exchange of volatiles among the atmosphere, polar caps, and regolith. Exchange of volatiles between the regolith and the atmosphere or cap may have been important in the past because the current atmosphere holds insufficient volatiles to account for a significantly larger former cap (Kieffer *et al.* 1992). During periods of low obliquity the variation in the average annual surface temperature with latitude is high, perennial ice caps form (Kieffer *et al.* 1992), and atmospheric pressure decreases. During periods of high obliquity, in contrast, the perennial ice cap decreases in size (Kieffer *et al.* 1992) and atmospheric pressure

increases. These temporal changes in the volume of the polar cap can lead to increases and decreases in loading of the underlying lithosphere.

Several lines of evidence point to a previously larger northern polar cap. First, the presence of outliers suggests that the cap may have extended southward at least to latitude 75°N. Second, as mentioned earlier, models in which viscous flow balances accumulation produce a best fit to polar cap topography for negligible accumulation rates and outward flow velocities of less than 1 mm per martian year, assuming a rheology appropriate to $H_2O$ ice (Zuber *et al.* 1998b). These models for cap dynamics suggest that the polar cap is either in steady state or decreasing in size at a very slow rate. Third, sublimation models matching the current cap shape indicate that the net effect of sublimation and condensation (for the present obliquity of Mars) is a northward retreat of the southern edges of the cap and growth of the cap at the pole (Ivanov and Muhleman 2000). Ivanov and Muhleman (2000) suggest that if the planetary obliquity had remained constant, the time scale for formation of the current polar cap shape is $10^6$ to $10^8$ yr. The effect of obliquity cycles over this time interval tends to favor the lower bound on the formation time, because the ice cap recedes rapidly during periods of high obliquity, but insufficient water ice is restored during periods of low obliquity (Ivanov and Muhleman 2000). Assumptions in the Ivanov and Muhleman model, however, engender caution against overinterpretation of the absolute time scales inferred.

Time scales for obliquity variations on Mars are difficult to infer, and the complexity of feedbacks between orbital variations and the solid-body response to climate changes may mean that there is no single "characteristic" time scale for obliquity variations. Individual obliquity cycles occur over periods of about $10^5$ yr (Touma and Wisdom 1993, Bills 1999). The similar time constants associated with the precession of the martian spin axis and precession of the orbit normal can lead to obliquity resonances, however, with time scales of $10^6$ yr (Bills 1999). In addition, feedback between the changing polar cap mass and planetary dynamics can occur. Unloading and loading of the lithosphere due to removal and reaccumulation of the present (Zuber and Smith 1999), or even a significantly larger (Bills 1999), polar cap in any individual obliquity cycle does not affect the planetary dynamics. However, phase lags in this feedback mechanism can result in long-term secular changes in the obliquity (Rubincam 1990, 1993; Spada and Alfonsi 1998; Bills 1999). Given all of these uncertainties, robust inferences on the long-term evolution of climate on Mars are not possible.

The above discussion indicates that, although current constraints on climate change time scales and associated changes in the size of northern polar cap are weak, significant changes in polar cap volume over periods of $10^6$ to $10^8$ years may have occurred. From our viscoelastic calculations, but only if the martian mantle has an Earth-like viscosity of $10^{21}$ Pa-s, the time scale for viscous response of the mantle to changes in cap loading is short compared with the time scale for producing those load changes. In contrast, if the martian mantle viscosity is as high as $10^{23}$ Pa-s, viscoelastic calcuations (Zhong and Zuber 2000) show that the time scale for viscous response of the mantle and the time scale for climate change could be comparable to within an order of magnitude. Under these conditions the present gravity and topography over the northern polar cap region would reflect the time-integrated interactions of loading history and lithospheric response.

## 7. CONCLUSIONS

We have employed elastic and viscoelastic models and altimetry and gravity data returned by the Mars Global Surveyor aerobraking hiatus and science phasing orbits to investigate the nature of isostatic compensation of the northern polar cap of Mars. Viscoelastic modeling suggests that the Maxwell time $\tau_m$ scales directly with mantle viscosity $\eta$, with $\tau$ ranging from $10^5$–$10^7$ yr for $\eta$ in the range $10^{21}$ (Earth-like) to $10^{23}$ Pa-s. Elastic plate models for compensation of the polar cap are valid if the time scales for climate-driven changes in the polar cap size are significantly longer than $\tau_m$. Under this premise the thickness of the effective elastic lithosphere and the density of the ice/rock mixture of the cap load control the cap thickness and volume and the temperature at the base of the cap. A thin elastic lithosphere beneath the polar cap results in greater subsidence beneath the cap, a larger cap volume, and higher basal temperatures than those of a thick elastic lithosphere. For a thin lithosphere and a polar cap containing a significant fraction of sediments, temperatures at the base of the cap may approach the melting point of cap material. Constraints on effective elastic lithosphere thickness are weak. If the Amazonian-aged circumpolar deposits fill a flexural depression surrounding the present cap, the effective elastic lithosphere thickness is in the range 60–120 km. Current analyses of gravity and topography (Phillips *et al.* 1999) are consistent with an elastic lithosphere thickness of 120 km for a crustal thickness of 50 km, although trade-offs among effective elastic lithosphere thickness, crustal thickness, and load density are permissive of other values for $T_e$. Interpretation of the gravity field in the northern polar region is difficult. One interpretation is that there is some correlation of gravity and topography over the central portion of the polar cap, but residual anomalies, uncorrelated with topography, over the remainder of the cap reflect lateral variations in crustal properties (Phillips *et al.* 1999). An alternative interpretation of the long-wavelength gravity field is that there has been relaxation of the longest wavelengths and that the remaining residual anomalies are at least in part unrelated to polar cap processes.

Current uncertainties in the viscosity of the martian mantle and in characteristic time scales for climate-driven changes in polar cap geometry allow the possibility that the time scales governing viscous relaxation and climate forcing are similar. This similarity would result in a complex and coupled loading history and lithospheric response, even for the modern polar

cap. Future work in many areas, including climate modeling, polar cap processes, and mantle dynamics, is needed to advance further our understanding of the effects of polar cap loading on the martian lithosphere.

## ACKNOWLEDGMENTS

We are grateful to the many instrument, spacecraft, and mission operations engineers who have contributed to the success of MGS and MOLA. We acknowledge thoughtful reviews by B. Bills and J. Weertman. This research has been supported by NASA Grants NAG5-4620 (C.L.J.), NAG5-4077 and NAG5-4436 (S.C.S.), NAG5-8263 (J.W.H.), NAG5-4448 (R.J.P.), and NAG5-4555 (M.T.Z.).

## REFERENCES

Banerdt, W. B. 1996. Support of long-wavelength loads on Venus and implications for internal structure. *J. Geophys. Res.* **91**, 403–419.

Batson, R. M., and E. Eliason 1995. Digital maps of Mars. *Photogram. Eng. Remote Sens.* **61**, 1499–1507.

Bills, B. G. 1999. Climate-rotation feedback on Mars. *Lunar Planet. Sci.* **30**, Abstract 1794. Lunar and Planetary Institute, Houston. [CD-ROM]

Blasius, K. A., J. A. Cutts, and A. D. Howard 1982. Topography and stratigraphy of martian polar layered deposits. *Icarus* **50**, 140–160.

Brotchie, J. F., and R. Sylvester 1969. On crustal flexure. *J. Geophys. Res.* **74**, 5240–5252.

Dial, A. L. J. 1984. Geologic map of the Mare Boreum region of Mars. U.S. Geological Survey Misc. Inv. Series Map I-1640.

Dzurisin, D., and K. Blasius 1975. Topography of the polar layered deposits of Mars. *J. Phys. Res.* **80**, 3286–3306.

Esposito, W. B., W. B. Banerdt, G. F. Lindal, W. L. Sjogren, M. A. Slade, B. G. Bills, D. E. Smith, and G. Balmino 1992. Gravity and topography. In *Mars* (H. H. Kieffer, B. M. Jakosky, C. W. Snyder, and M. S. Matthews, Eds.), pp. 209–248. Univ. of Arizona Press, Tucson.

Fishbaugh, K., and J. W. Head 1999. North polar region of Mars: Topography of circumpolar deposits from Mars Orbiter Laser Altimeter (MOLA) data and evidence for asymmetric retreat of the polar cap. *J. Geophys. Res.*, submitted.

Fletcher, N. H. 1970. *The Chemical Physics of Ice.* Cambridge Univ. Press, New York.

Head, J. W., M. Kreslavsky, H. Hiesinger, M. Ivanov, S. Pratt, N. Siebert, D. E. Smith, and M. T. Zuber 1998. Oceans in the past history of Mars: Tests for their presence using Mars Orbiter Laser Altimeter (MOLA) data. *Geophys. Res. Lett.* **25**, 4401–4404.

Hobbs, P. V. 1974. *Ice Physics.* Oxford Univ. Press, London.

Hooke, R. L. 1998. *Principles of Glacier Mechanics*. Prentice Hall, New Jersey.

Ivanov, A. B., and D. O. Muhleman 2000. The role of sublimation for the formation of the northern ice cap: Results from Mars Orbiter Laser Altimeter. *Icarus* **144**, 436–448.

Kieffer, H. H., and A. P. Zent 1992. Quasi-periodic climate change on Mars. In *Mars* (H. H. Kieffer, B. M. Jakosky, C. W. Snyder, and M. S. Matthews, Eds.), pp. 1180–1218. Univ. of Arizona Press, Tucson.

Konopliv, A. S., and W. L. Sjogren 1995. The JPL Mars gravity field, Mars50c, based upon Viking and Mariner 9 Doppler tracking data. Publ. 95-5. Jet Propulsion Lab., Pasadena, CA.

Kraus, H. 1967. *Thin Elastic Shell Theory*. Wiley, New York.

Lemoine, F. G., D. D. Rowlands, D. E. Pavlis, D. S. Chinn, S. B. Luthke, G. A. Neumann, and D. E. Smith 1999. Precise orbit determination for Mars Global Surveyor duringhiatus and SPO. *Bull. Am. Astron. Soc.* **99**, 147.

Malin, M. C. 1986. Density of martian northern polar deposits: Implications for composition. *Geophys. Res. Lett.* **13**, 444–447.

McNutt, M. K. 1984. Lithospheric flexure and thermal anomalies. *J. Geophys. Res.* **89**, 11,180–11,194.

Phillips, R. J., R. M. Williams, M. T. Zuber, G. A. Neumann, D. E. Smith, C. L. Johnson, S. C. Solomon, and W. L. Sjogren 1999. Gravity-topography relationships in the northern polar region of Mars. *Eos Trans. Am. Geophys. Union* **80**, Spring Meeting Suppl., S202.

Rowlands, D. D., D. E. Pavlis, F. G. Lemoine, G. A. Neumann, and S. B. Luthke 1999. The use of laser altimetry in the orbit and attitude determination of Mars Global Surveyor. *Geophys. Res. Lett.* **26**, 1191–1194.

Rubincam, D. P. 1990. Mars: Change in axial tilt due to climate? *Science* **248**, 720–721.

Rubincam, D. P. 1993. The obliquity of Mars and "climate friction." *J. Geophys. Res.* **98**, 10,827–10,832.

Smith, D. E., and M. T. Zuber 1996. The shape of Mars and the topographic signature of the hemispheric dichotomy. *Science* **271**, 184–188.

Smith, D. E., F. J. Lerch, R. S. Nerem, M. T. Zuber, G. B. Patel, S. K. Fricke, and F. G. Lemoine 1993. An improved gravity field model for Mars: Goddard Mars model 1. *J. Geophys. Res.* **98**, 20,871–20,899.

Smith, D. E., W. L. Sjogren, G. L. Tyler, G. Balmino, F. G. Lemoine, and A. S. Konopliv 1999. The gravity field of Mars: Results from Mars Global Surveyor. *Science* **286**, 94–97.

Smith, D. E., M. T. Zuber, H. V. Frey, J. B. Garvin, J. W. Head, D. O. Muhleman, G. H. Pettengill, R. J. Phillips, S. C. Solomon, H. J. Zwally, W. B. Banerdt, and T. C. Duxbury 1998. Topography of the northern hemisphere of Mars fom the Mars Orbiter Laser Altimeter. *Science* **279**, 1686–1692.

Spada, G., and L. Alfonsi 1998. Obliquity variations due to climate friction on Mars: Darwin versus layered models. *J. Geophys. Res.* **103**, 28,599–28,605.

Squyres, S. W., S. M. Clifford, R. O. Kuzmin, J. R. Zimbleman, and F. M. Costard 1992. Ice in the martian regolith. In *Mars* (H. H. Kieffer, B. M. Jakosky, C. W. Snyder, and M. S. Matthews, Eds.), pp. 523–554. Univ. of Arizona Press, Tucson.

Tanaka, K. L., and D. D. H. Scott 1987. Geologic map of the polar regions of Mars. U.S. Geological Survey Misc. Inv. Series Map I-1802-C.

Tanaka, K. L., D. D. H. Scott, and R. Greeley 1992. Global stratigraphy. In *Mars* (H. H. Kieffer, B. M. Jakosky, C. W. Snyder, and M. S. Matthews, Eds.), pp. 345–382. Univ. of Arizona Press, Tucson.

Thomas, P. T., S. Squyres, K. Herkenhoff, A. Howard, and B. Murray 1992. Polar deposits of Mars. In *Mars* (H. H. Kieffer, B. M. Jakosky, C. W. Snyder, and M. S. Matthews, Eds.), pp. 767–795. Univ. of Arizona Press, Tucson.

Touma, J., and J. Wisdom 1993. The chaotic obliquity of Mars. *Science* **259**, 1294–1297.

Turcotte, D. L., R. J. Willemann, W. F. Haxby, and J. Norberry 1981. Role of membrane stresses in the support of planetary topography. *J. Geophys. Res.* **86**, 3951–3959.

Willemann, R. J., and D. L. Turcotte 1981. Support of topographic and other loads on the Moon and on the terrestrial planets. *Proc. Lunar. Planet. Sci. Conf. 12th*, 837–851.

Wu, S. S. C. 1989. Topographic maps of the western, eastern equatorial and polar regions of Mars, Scale 1:15,000,000. U.S. Geological Survey Misc. Inv. Series Map I-2030.

Wu, S. S. C. 1991. Topographic maps of the polar, western and eastern regions of Mars, Scale 1:15,000,000. U.S. Geological Survey Misc. Inv. Series Map I-2160.

Zhong, S. 1997. Dynamics of crustal compensation and its influences on crustal isostasy. *J. Geophys. Res.* **102**, 15,287–15,299.

Zhong, S., and M. T. Zuber 2000. Long-wavelength topographic relaxation for self-gravitating planets and implications for the time-dependent compensation of surface topography. *J. Geophys. Res.*, in press.

Zuber, M. T., and D. E. Smith 1999. Effect of Mars's present-day north polar cap on the moment of inertia and planetary dynamics. *Lunar Planet. Sci.* **30**, Abstract 1589. Lunar and Planetary Institute, Houston. [CD-ROM]

Zuber, M. T., D. E. Smith, R. J. Phillips, S. C. Solomon, W. B. Banerdt, G. A. Neumann, and O. Aharonson 1998a. Shape of the northern hemisphere of Mars from the Mars Orbiter Laser Altimeter (MOLA). *Geophys. Res. Lett.* **25**, 4393–4396.

Zuber, M. T., D. E. Smith, S. C. Solomon, J. B. Ashire, R. S. Azfal, O. Aharonson, K. Fishbaugh, P. G. Ford, H. V. Frey, J. B. Garvin, J. W. Head, A. B. Ivanov, C. L. Johnson, D. O. Muhleman, G. A. Neumann, G. H. Pettengill, R. J. Phillips, X. Sun, H. J. Zwally, W. B. Banerdt, and T. C. Duxbury 1998b. Observations of the north polar region of Mars from the Mars Orbiter Laser Altimeter. *Science* **282**, 2053–2060.